BNL-220997-2021-JAAM

Resolving the evolution of atomic layer deposited thin film growth by continuous in situ X-ray absorption spectroscopy

X. Qu, M. Liu

To be published in "Chemistry of Materials "

February 2021

Center for Functional Nanomaterials

Brookhaven National Laboratory

U.S. Department of Energy

USDOE Office of Science (SC), Basic Energy Sciences (BES) (SC-22)

DISCLAIMER

Resolving the evolution of atomic layer deposited thin film growth by continuous *in situ* X-ray absorption spectroscopy

Xiaohui Qu[†], *Danhua Yan*[†,§], *Ruoshui Li*[†,⊥], *Jiajie Cen*[§], *Chenyu Zhou*[†,§], *Wenrui Zhang*[†], *Deyu Lu*[†], *Klaus Attenkofer*[‡], *Dario J. Stacchiola*[†], *Mark S. Hybertsen*[†,*], *Eli Stavitski*[‡,*], *and Mingzhao Liu*[†,*]

[†]Center for Functional Nanomaterials and [‡]National Synchrotron Light Source II, Brookhaven National Laboratory, Upton, New York 11973, United States

[§]Department of Materials Science and Chemical Engineering and [⊥]Department of Chemistry, Stony Brook University, Stony Brook, New York 11794, United States

Abstract

In situ synchrotron X-ray absorption near edge structure characterization of thin film titania growth by atomic layer deposition (ALD) over ZnO nanowires reveals persistent low-coordinated Ti motifs leading to a new picture of ALD growth. Through design of the growth and measurement cycles, Ti *K*-edge spectral data are continuously recorded so as to characterize the film evolution as a function of ALD cycle number and the surface changes within the time scale of the ALD cycle. A unified set of analysis tools are developed to interpret the time-series of spectral data. A prenucleation stage of growth, a transition region, and then a steady state growth stage are observed with distinguishable features. Multivariate curve resolution analysis, physically constrained, demonstrates two specific spectral components with associated, time-dependent concentrations. The bulk film component tracks the stages of growth. The surface and interface component, present throughout the stages of the growth, reveals a significant coverage of relatively isolated or loosely networked tetrahedrally-coordinated Ti atomic motifs. Finally, spectral signatures for the intra-cycle growth kinetics are reconstructed at a time resolution of ~ 1s and demonstrate that transient Ti motifs on the growing surface stabilize within a few seconds of the Ti precursor pulse.

Introduction

Developed and extensively studied during the past two decades, atomic layer deposition (ALD) is a unique type of chemical vapor deposition (CVD) for thin film fabrication.[1-3] Compared to other vapor phase deposition techniques, ALD stands out for growth of films with superior uniformity that can conformally coat non-planar surfaces and it exhibits precise control over film thickness at relatively low processing temperatures.[4] These advantages stem from the self-limiting and periodic nature of the ALD process. The two vapor phase precursors are alternatively introduced into the growth chamber, forming successive self-assembled monolayers through chemisorption and controlled reactions.[5] The newly introduced precursor vapor of one type reacts with the chemisorbed species derived from the precursor of the other type deposited immediately prior. This limits the deposition of thin film material over one full ALD cycle to a single monolayer or submonolayer, depending on the precursor footprint.[6] Thus, sequential control of surface reactions and near-equilibrium conditions enable the highly uniform and conformal ALD growth. Over the years, ALD has seen a wide range of applications in microelectronics,[7] catalysis,[8] solar energy harvest,[9] and biomedical fields.[10]

Ideally, the ALD growth proceeds in a linear regime throughout the film growth with the same quantity of material added during each cycle, monolayer by monolayer. In practice, growth rates can be considerably slower, with a fraction of a monolayer grown during each cycle, depending on factors such as the size of the precursor. In addition, similar to other vapor phase deposition techniques, a nucleation process is inevitable at the beginning of deposition. The first few ALD cycles may result in an initial growth morphology that is different from the bulk of the film.[11-13]

Establishing consistent, near-equilibrium chemisorption of the precursors requires fine tuning of deposition conditions through trial-and-error. In recent years, a few lab-based and synchrotron-based *in situ* techniques[14], including quartz crystal microbalance (QCM)[15], spectroscopic ellipsometry[16, 17], vibrational spectroscopy[5, 18], and X-ray fluorescence (XRF)[13,

[19, 20], have been applied to monitor ALD growth for real-time diagnostics. This enables greater control over the growth rate and quality of the films. However, each of the available techniques has its own limitations. For example, QCM only reports the growth rate on the microbalance surface, which may not have the same temperature or surface condition as the growth substrate. Spectroscopic ellipsometry reports both film thickness and optical constants, where the latter may be used to infer film quality. However, it is applicable only for smooth, flat substrates. It cannot be used to monitor film growth over complex, 3D structures. Finally, while vibrational spectroscopy offers insight into the surface reaction kinetics, it does not quantify the thickness of the growing thin film.

Here, we report advances in the *in situ* monitoring of ALD film growth over complex, 3D nano-architectures using synchrotron X-ray absorption near edge structure (XANES) spectroscopy. Due to the specific onset energies of the X-ray absorption edges associated with excitation of electrons from atomic core-levels, XANES is element-specific and the shifts in the absorption edge correlate to the atomic valence. Furthermore, the final state electron undergoes multiple scattering from neighboring atoms resulting in spectroscopic signatures that are sensitive to the structural details of the neighboring atomic shells.[21, 22] The binding energy of the transition metal *K*-shell typically falls in the hard X-ray range resulting in a large material penetration depth (> 10 μm). Thus, the technique is very suitable for studies of a broad array of important thin film materials, capturing information from the entire film. On the other hand, to monitor the evolution of local structure motifs through different phases of growth, measurements must be executed throughout the growth. To date, there has been important progress using *in situ* XANES to study ALD thin film growth, so far focusing on quasi-steady state conditions between precursor pulses during early growth cycles, often with intermittent pauses in the ALD growth process.[20, 23-30] We also note that other synchrotron-based techniques have been previously applied to monitor several materials growth techniques *in situ*, including

organometallic vapor-phase epitaxy[31], molecular beam epitaxy[32-34], and atomic layer deposition[28, 35-37].

In the present work, we demonstrate that XANES data can be collected continuously during the ALD process, supplying a sequence of data probing the growth process in all stages. We specifically focus on ALD growth of titania thin film coatings over ZnO nanowires. Previously, we have established optimized growth conditions and then used *ex situ* XANES studies to characterize the titania films, finding that they are largely amorphous and contain a substantial fraction of under-coordinated Ti^{4+} ions.[38, 39] Leveraging the high photon flux and sensitivity of the Inner Shell Spectroscopy (ISS) beamline at National Synchrotron Light Source II (NSLS II) and a dedicated, fully integrated ALD reactor, we investigate the structural evolution of the titania coating *in situ* as it accumulates under growth conditions similar to those that were previously optimized.

By tuning precursor injection interval and XANES scan period, we are able to collect approximately two full Ti *K*-edge XANES spectra per ALD cycle and overall, accumulate more than 600 spectra over the growth of about 6 nm of titania. In the analysis of the data, we are able to characterize features of the growth, both as they evolve over all the stages of the growth and on the short, intra-cycle time scale. This is achieved by deploying a set of data analysis techniques to treat the full time-sequence of spectral data in a unified manner. The data reveal a growth sequence starting with an approximately linear prenucleation stage, a non-linear transition stage and then the final steady-state, linear ALD growth stage. The analysis also enables us to distinguish a surface/interface component of the ALD titania layer characterized by either relatively isolated or lower density, loosely networked tetrahedral-coordinated Ti atomic motifs. These motifs appear during the prenucleation stage and persist on the growing surface throughout the ALD cycles, suggesting an important role in the growth process. Finally, the concentration of new Ti deposited during a single ALD cycle, and the essential structure

motifs formed, stabilize within a few seconds under the current growth conditions. Synthesis of our observations leads to a new picture for the ALD growth of titania.

Results and Discussions

In situ ALD XANES measurements

The *in situ* ALD XANES measurement set-up is shown schematically in Figure 1a. An ALD growth reactor is integrated into the beamline operations. This includes the photon delivery system and the fluorescence detection, as well as the controls system which records the time-stamps of the ALD precursor pulses. For the growth sequence measured here, precursor vapors of titanium isopropoxide (TTIP) and water are alternately introduced into the chamber as short pulses. Between the precursor pulses, a uniform pulse-to-pulse duration is set to ensure the complete purge of one precursor from the gas phase before the introduction of another. This cycle is shown schematically in Figure 1b. Detailed processing parameters appear in the Methods section.

A silicon wafer covered with vertical, single crystalline ZnO nanowires (NWs) is chosen as the model nano-architectured substrate (Supporting Information, Figure S1). The growth conditions used here are similar to our previously optimized procedures for this system.[38] After a total of 320 ALD cycles at 150ºC, a uniform, 6 nm-thick coating of TiO_2 is formed over the ZnO nanowires, as shown by the transmission electron microscopy (TEM) image (Supporting Information, Figure S1, inset). The nominal growth rate per cycle of 0.019 nm cy^{-1} (1 cy = 1 ALD cycle) is close to the reported value (~0.02 nm cy^{-1}) for self-limiting ALD growth of TiO_2 using TTIP and water precursors.[40, 41] A XANES spectrum collected at the end of TiO_2 ALD clearly reveals an amorphous structure, fully consistent with the conclusion of our previous *ex situ* study (Supporting Information, Figure S2).[38] The clear similarity between the spectra measured *ex situ* previously and *in situ* in the present study suggests that we have minimal X-ray beam effects during the *in situ* study.

During the ALD growth sequence, *in situ* Ti *K*-edge XANES spectra (4920 – 5140 eV) are collected continuously. There is no interruption to the growth process. The Ti *K*-edge X-ray absorption is determined by measuring the total X-ray fluorescence yield, i.e., $\mu(E) = I_f/I_0$, in which I_0 and I_f are respectively the intensities of the incident beam and the X-ray fluorescence. The Ti *K*-edge absorption specifically probes the amount of Ti illuminated by the beam. Naturally, this provides the atomic specificity to probe the growing titania shell. However, for the short, intra-cycle time period, Ti precursor vapor (TTIP) is also in the growth chamber where it can contribute to the signal. In the data analysis process, the contribution from the vapor is detected and removed. The magnitude of the edge jump in the spectra $\mu(E)$ quantifies the thickness of TiO_2 shell as it is deposited. Where needed, spectra are normalized for comparison.

To optimize spectral quality while minimizing the time to acquire a complete spectrum, a unique spectral collection mode is adapted at the beamline. The energy of the monochromatized incident beam is scanned across the spectral range at a non-uniform rate, following a predetermined trajectory that is repeated throughout the ALD process (Figure 1c). The trajectory is optimized to achieve a slower scanning rate in the spectral region near the absorption edge (4960 – 5000 eV) where higher signal-to-noise ratio is most important while allowing faster scanning outside that range.

The period of XANES collection (T_X) is chosen based on signal-to-noise considerations across the growth sequence as well as seeking to resolve features of the growth within the time scale of the ALD cycle (T_A). These constraints lead us to set T_X to be roughly half of T_A. Because the time scales are comparable, the collected data set must be considered at the level of the individual monochromator settings as a function of time. In other words, the spectrum is collected using monochromatized light dwelling on one photon energy $E_i = E(t_i)$ for a short interval centered at each time $t = t_i$, programmed as illustrated in Figure 1c. As a function of

time, the sample is in principle characterized by a spectrum that depends on the state of the sample, as represented by a bivariate spectral function, $\mu(E,t)$. As a result of the measurement procedure, this bivariate function is only being sampled at one discrete photon energy E_i at time t_i. Therefore, the data set is a 1-dimensional time series, $\mu(E_i,t_i)$.

The data analysis protocols we develop here handle this extra complication. We are able to monitor the cycle-to-cycle time evolution of the ALD film growth from the nucleation stage through film completion. In addition, the choice of the T_X/T_A ratio is exploited to give us fast time resolution to probe characteristics of the growing film within the ALD cycle. Within each ALD cycle k, we define an intra-cycle delay time $\tau \in [0,T_A)$ to be $\tau = t - kT_A$. In particular, provided the T_X/T_A ratio is chosen distinct from any simple rational fraction, over the course of a large number of ALD cycles, spectral intensity for each photon energy $E(t_i) = E(kT_A+\tau_i)$ will be obtained by probing a grid of intra-cycle delay time points τ_i within the ALD cycle k. This can be seen schematically from Figure 1c as the XANES cycle is shifting with respect to the ALD cycle. The data analysis protocols exploiting this will be described below, including discrimination of the contribution of the vapor phase precursor. First, we analyze the XANES measurements across the full time-scale of the film growth.

Stages of titania ALD growth

Here we present the XANES measurements split according to the ALD cycle number into a sequence $\{\mu_k(E)\}$ that approximates the mean XANES spectrum during cycle k. For this data set, T_X = 70.49 s is slightly longer than $T_A/2$ (60.53 s). All photon energies are sampled at least once per ALD cycle and most are sampled twice. We accumulate all of the spectral data in the time window defined by the period between eight seconds after the start of the k^{th} TTIP pulse and the start of the $(k+1)^{th}$ pulse, averaged as appropriate to get $\mu_k(E)$. The analysis below will show that the transient signal from Ti is contained within the first eight seconds of the ALD cycle, including the contribution of the gas phase precursor. Our procedure for $\{\mu_k(E)\}$

eliminates this contribution. Other intra-cycle variations will not affect this portion of the analysis. The resulting sequence of spectra are shown in Figure 2a with a perspective that emphasizes the emerging spectral features. Qualitatively, the spectra appear similar from the beginning of the deposition to the end at $k = 320$. By comparing a sampling of the spectra across the growth sequence, it is apparent that early in the growth, the pre-edge feature is enhanced and the initial portion of the white line is suppressed compared to later in the growth when the bulk of the film dominates (Supporting Information, Figure S3).

The alternative perspective on the data set shown in Figure 2b highlights the kinetics of the film growth. Here, we plot $\mu_k(E)$ against k for each energy E. It is qualitatively apparent across the spectral range that there are two kinetic stages, both showing relatively stable, linear growth rates. Stage I ($k < \sim 75$) is significantly slower than Stage II ($k > \sim 143$). Generally, in the high energy range of XANES, the X-ray absorption spectrum exhibits weaker dependence on the chemical environment of the atom.[21] An average in this range is simply proportional to the number of atoms in the sample. For the present Ti *K*-edge data, we therefore calculate the edge jump for each spectrum from the average spectral strength within the 5100 – 5140 eV energy window to use as a metric for average titania film thickness. From *ex situ* measurements, the TiO_2 layer accumulates to a thickness of 6 nm at the end of 320 ALD cycles, allowing us to convert the measured edge jump to a thickness scale. The resulting growth profile is shown in Figure 3a. This shows the qualitative features we noted in Figure 2a.

Quantitatively, we determine growth per cycle values of 0.006 nm cy^{-1} and 0.025 nm cy^{-1} respectively for Stage I and Stage II. These growth rates show that in Stage II, the ALD growth of titania reaches the steady, linear regime previously established for the precursors TTIP and H_2O.[40, 41] In Stage I the growth rate is much slower, likely due to kinetic limitations in the initial formation of titania clusters on ZnO up to an average accumulated thickness of about 0.5 nm. Between the two stages, there is an intermediate period where the growth is nonlinear with respect to the number of ALD cycles.

For the first few ALD cycles, the detector noise prevents quantitative assessment of the early stage directly from the spectra without further data processing (Supporting Information, Figure S3). Also, more generally, as the growth proceeds, the spectrum at each cycle k averages over the full thickness of the film grown to that point. This motivates us to define a *differential spectrum*, $\Delta\mu_k(E) = \mu_k(E) - \mu_{k-1}(E)$, as a spectral characteristic of the per-cycle deposition of Ti at the k^{th} cycle. Within a linear growth regime, each ALD cycle adds the same amount of identical material. We may therefore perform linear regression of the data set $\{\mu_k(E)\}$ with respect to the cycle number k in each stage. This determines $\Delta\mu(E)$ energy by energy from the slope term as a statistical mean of $\Delta\mu_k(E)$ for this stage.

The differential spectra in Stages I and II, namely $\Delta\mu^{\text{I}}(E)$ and $\Delta\mu^{\text{II}}(E)$, closely resemble XANES spectra of TiO_2 film during growth (Supporting Information, Figure S3), but exhibit significantly higher signal-to-noise ratio, as shown in Figure 3b. Edge jump normalized spectra (Figure 3c) show overall similarity, but $\Delta\mu^{\text{I}}(E)$ clearly features a sharper and higher pre-edge peak at 4968 eV than $\Delta\mu^{\text{II}}(E)$. In addition, the doublet feature in the white line region of $\Delta\mu^{\text{II}}(E)$ appears merged in $\Delta\mu^{\text{I}}(E)$. During the nonlinear transition period, the differential spectra are found to be fully captured by an interpolation between $\Delta\mu^{\text{I}}(E)$ at its beginning and $\Delta\mu^{\text{II}}(E)$ at its end. The measured spectra can be reconstructed form the interpolated differential spectra (Supporting Information, Figure S4), so no distinct new spectral features emerge within the transition period. Naturally, the same analysis applies to the growth profile. It can be reconstructed by interpolating the measured linear growth rates from Stages I and II (Supporting Information, Figure S4).

During Stage II, the total spectrum at a snapshot in time derives primarily from Ti atoms in the bulk of the film, with smaller contributions from those at the interface to ZnO and those on the outer surface. In the controlled reaction picture for a cycle of ALD growth, the local Ti structure motifs on the surface are relatively steady from one cycle to next. In Stage II, at the

low temperatures of the growth considered here (150 ºC), the Ti structure motifs at the buried interface should be frozen. Therefore, the surface and the buried interface make little contribution to the differential XANES spectrum. As a result, $\Delta\mu(E)$ is entirely attributed to volume increase of the Ti atoms representative of the bulk of the thin film. In other words, the differential spectra in Stage II are sensitive to the Ti atoms that are effectively being incorporated into bulk-like structure motifs by surface reactions that are covering them with fresh surface motifs. This picture is confirmed by comparing the spectral form of $\Delta\mu^{\mathrm{II}}(E)$ to the XANES spectrum collected at the end of ALD cycles (k = 320). At a 6 nm film thickness, the latter spectrum is dominated by the bulk of the film. As seen in Figure 3d, the differential spectrum in Stage II is essentially identical to that of the bulk film.

On the other hand, during Stage I, the interface and surface motifs are just developing, each with characteristic motifs. Added Ti atoms are contributing to these motifs and $\Delta\mu^{\mathrm{I}}(E)$ is mostly attributed to the accumulation of titania clusters on the ZnO surfaces. The Stage I differential spectra show a more prominent pre-edge peak (4970 eV) together with some suppression of the first main feature in the white line region of the spectrum (4990 eV). This is discussed further below.

In order to specifically discriminate the characteristics of the bulk of the film from those of the interface and outer surface, we employ multivariate curve resolution with alternating least squares algorithm (MCR-ALS).[42, 43] This technique is a commonly adapted chemometric tool developed to extract the chemical structure and kinetics information from time series spectroscopy data,[44] including *in situ* and operando XANES data in recent years.[45-47] The analysis assumes that the measured spectra derive from a small number of invariant constituent, contributing spectra. Only the concentration of each constituent is varying in time. The MCR-ALS algorithm achieves the decomposition of the time sequence spectral data set into individual component spectra and their respective concentration profiles without the need of reference spectra.[43] However, it is also well documented that this powerful approach can exhibit

ambiguity due to rotations within the solution space that may result in mathematically equivalent solutions.[48] Therefore, achieving physically meaningful solutions may require proper constraints based on prior knowledge. Finally, the algorithm can only distinguish those components of the signal that have a distinct time evolution.

In applying MCR-ALS to the data gathered for the full growth sequence (Figure 2), we need to identify the number of components that can be robustly extracted. After initially considering the three terms that one expects physically (bulk, interface, and surface), we conclude that the characteristics of the interface and surface components are too similar to be disentangled. Furthermore, by the end of the growth sequence, those components are small compared to the bulk component. We settle on two components that emerge to be bulk and a composite we designate as surface/interface. Another factor concerns the signal-to-noise ratio, particularly in the spectra taken for the first few ALD cycles. Finally, we also apply smoothness constraints to both bulk and surface/interface concentration evolution (Methods section). This reflects the hypothesis that the accumulation of film *bulk* and *surface/interface* species are continuous.

The final MCR-ALS analysis is applied to the XANES data set $\{\mu_k(E)\}$ starting from ALD cycle $k = 57$, *i.e.*, starting from a point late in Stage I and extending through the entire transition period and Stage II. This choice meets the needs of signal-to-noise ratio and distinguishable temporal evolution. The deconvoluted spectra of the two species and their respective MCR concentrations are presented in Figures 4a and 4b. In the present context, the concentration of each species is converted to equivalent thickness using the final film thickness of 6 nm, as noted above.

We perform consistency tests to assess the MCR results. First, the MCR spectra and concentrations are used to numerically reconstruct differential spectra. These are then compared to the differential spectra deduced in the separate analysis above. The results agree very well (Supporting Information, Figure S5). Second, the spectra from early in Stage I that

are excluded from the MCR analysis, are fully accounted for by linear combinations of the constituent spectra from MCR (Supporting Information, Figure S6). These tests strongly indicate that just two distinguishable spectra form the basis for the XANES cycle-to-cycle data set $\{\mu_k(E)\}$.

Based on their concentration evolution profiles, the two deconvoluted components are respectively assigned to *bulk* and *surface/interface* species (Figure 4b). The major, bulk component grows with a profile that is similar to the overall time evolution observed in Figures 2 and 3a. The associated spectrum is essentially identical to that found in the differential analysis and measured at the end of the growth (Figure 3d). The bulk component, not surprisingly, locks in very robustly since it dominates in the Stage II growth. There are only small fluctuations around the smooth profile constraint.

The minor, surface/interface component has a much smaller equivalent thickness, less than 0.2 nm. This component is a significant part of the signal during Stage I growth and early in the transition region (Figure 4b). Here, the overall signal is relatively low and noise has considerable impact. The use of the smoothness constraint assists in obtaining a stable result for the associated spectrum. Large fluctuations in the raw values of the deduced concentration are evident. During Stage I and transition, the equivalent thickness of the surface/interface component first increases to a maximum of 0.18 nm at about ALD cycle 170. Then, as the growth proceeds in Stage II, it slowly decreases, approaching a plateau at 0.16 nm after about 270 ALD cycles. The equivalent thickness of the surface/interface component approximately corresponds to 0.5 monolayer (ML) of TiO_2. The thickness of 1 ML TiO_2 is defined as the *c*-axis length of a rutile TiO_2 unit cell (0.30 nm).

The associated spectrum qualitatively differs from the bulk spectrum (Figure 4a). Key features, namely the enhanced pre-edge feature and the suppression of the lower energy component in the while line region, are similar to those observed in the differential spectrum in Stage I, but even more pronounced. Interestingly, the surface/interface spectrum bears a strong

resemblance to the Ti *K*-edge XANES of titanosilicates-1 (TS-1, Figure 4c) and other dilute TiO_2-SiO_2 aerogels, which have a high abundance of isolated tetrahedral Ti sites specifically.[49-51] The same pattern is also observed from a simulated spectrum in our earlier report for a structure with loosely packed Ti_{4c} sites (Supporting Information, Figure S7).[38, 39]

The relative contributions of the bulk and surface/interface components identified in the MCR analysis are plotted in Figure 4d, as percentage fractions of the film as a function of growth cycle. The thin lines show the fractions deduced from raw concentrations, while the bold lines are based on smoothed profiles from MCR. We also extend the analysis back into the earlier portion of the data in Stage I, prior to the starting point of the MCR analysis, k = 57. First, linear regression is applied to the differential spectrum in Stage I. We find that $\Delta\mu^{\mathrm{I}}(E)$ is accurately fit by 29% surface/interface component and 71% of bulk component. Second, linear regression is applied to the individual spectra with the results plotted as light dashed lines. Finally, to assess the trend in this noisy data, the concentrations deduced from the individual spectra are fit to a linear concentration profile, resulting in the smoothed profiles of percentage fractions shown by the bold dashed lines. These results for $k < 57$ are consistent with the average result from the differential spectrum and with the MCR analysis near $k = 57$, as shown in Figure 4d. While there is impact of the noise in stage I, the overall evolution over the stages of growth emerges in Figure 4d. In particular, the bulk spectrum is clearly discernible as a component early in Stage I.

Intra-cycle kinetics of titania ALD

The differential and MCR-ALS analyses of the cycle-to-cycle XANES data set $\{\mu_k(E)\}$ together show that in addition to the bulk signal, a single, distinguishable surface/interface spectrum explains the entire evolution of the measured spectra on this coarse-grained time scale. This supports the hypothesis articulated in the previous section: on the average, the distribution of the essential, Ti-centered structure motifs at the surface are the same across the ALD cycles.

We now use this assumption to analyze the XANES data set $\mu(E_i, \tau_i)$ to extract spectral signatures with a time resolution of ~1 second, specifically within the ALD cycle.

Figure 5a further develops the interplay between the XANES measurement cycles and the ALD growth cycles. Given an ALD process with period T_A, we may write time t as $t_i = kT_A + \tau_i$, where k is the cycle number and $\tau_i \in [0, T_A)$ is the delay time from the k^{th} cycle start (TTIP pulse). Within each ALD cycle, we rewrite $\mu(E_i, t_i)$ in the general form of

$$\mu(E_i, t_i = kT_A + \tau_i) = \mu_k^s(E_i) + g(E_i, \tau_i), \quad (1)$$

in which $\mu_k^s(E)$ is the XANES spectrum at the *end* of k^{th} cycle, while $g(E, \tau)$ describes transient spectral features associated with varying Ti-centered motifs due to intra-cycle kinetics. The ALD cycle (Figure 1b) starts with the injection of additional Ti into the reactor through the TTIP pulse, so we expect that $g(E, \tau)$ will be most significant in the early times τ right after the TTIP pulse. On the other hand, it must have an asymptotic behavior $g(E, \tau) \to 0$ approaching the end of the ALD cycle where $\mu_k^s(E)$ represents the spectrum. Furthermore, with the relatively long ALD cycle time chosen in this study, the final data will be consistent with $g(E, \tau)$ being indistinguishable from background for most of the time period $\tau > T_A/2$, after the H_2O pulse. Then, following the approach visualized in Figure 5a, a spectral data point measured in the second half of the pulse is used as the reference to deduce a data point for the differential spectrum $g(E, \tau)$. As noted, with the assumption of invariance across the ALD cycles, this data is accumulated and averaged to form the final representation of $g(E, \tau)$, as detailed further in the Methods section.

In Figure 5b, the accumulated data set for the transient spectrum, $g(E_i, \tau_i)$, is plotted as a 2D map in the delay time range of $\tau = 0 - 15$ s. (The full range plot is shown in the Supporting Information, Figure S9.) The noise level reflects the fact that spectra represent the signal from a submonolayer concentration of Ti. Despite the noise, the spectral features corresponding to Ti *K*-edge XANES emerge in the first few seconds after TTIP pulse ($\tau \leq 5$ s), with a clear

absorption edge near 4980 eV. Due to the scarcity of data available for the 2D mapping, $g(E_i, \tau_i)$ data are obtained from all available ALD cycles, without distinguishing the growth stages. As such, the transient spectrum represents intracycle kinetics averaged across the entire process.

In Figure 5c, the data set $g(E_i, \tau_i)$ is binned in a series of time windows and then plotted as spectra. These are differential spectra that specifically probe the dynamics of Ti motifs relative to the stable motifs near the end of the cycle. In particular, a net edge jump indicates additional Ti atoms relative to the reference portion of the ALD cycle after the H_2O pulse. The first time window (0.2- 2.5 s) is chosen due to the emergence of a very sharp pre-edge feature. The full Ti *K*-edge spectrum shows a more prominent pre-edge feature than typically observed for solids. The transient spectrum for the first time window in Figure 5c is compared to a reference spectrum measured for the TTIP vapor phase (Supporting Information, Figure S10a). This shows that the transient species in this time window are TTIP molecules in the gas phase or loosely attached to the surface via physisorption. The spectrum in the second time window (2.5 – 5 s) still indicates a net edge jump, but the details in this differential spectrum are not easily interpreted relative to the noise. In the final time window, integrating from 5 s up to just prior to the H_2O pulse, there is no longer a discernable edge jump and noise dominates. In particular, there are no spectral features in this time window that would indicate a significant change in the structures of the Ti centered motifs on the surface, relative to those on the surface after the H_2O pulse, within the sensitivity of the measurement.

To further quantify the evolution of the additional Ti concentration probed here within the first half of the ALD cycle, the data set $g(E_i, \tau_i)$ is binned across the spectral window (5050 – 5150 eV) and the integrated spectral weight is shown as a function of τ in Figure 5d. The concentration of transient Ti-species rises quickly (within 1 s) after the TTIP pulse and decays to the background level after $\tau = 5$ s. Subsequently, the amount of added Ti on the surface

remains approximately constant. We can also conclude that the Ti concentration remains constant during the second half of the ALD cycle, following the H_2O pulse.

Discussion of titania ALD growth

Our *in situ* XANES data (Figure 3a) indicate that the ALD growth initiates with a slow, essentially linear Stage I growth period (0.006 nm cy^{-1}) before transitioning to the more rapid Stage II growth (0.025 nm cy^{-1}) characteristic of self-limiting ALD growth of TiO_2 using TTIP and water precursors. The presence of a slower, prenucleation stage prior to the steady growth has been observed in ALD growth for other materials, most recently by Skopin and coworkers through an *in situ* XRF study on ZnO ALD.[13] According to their report, the slower growth is attributed to the formation of a highly amorphous adsorption layer with few nucleation clusters.

Here, we observe linear growth in Stage I, up to the nominal film thickness of 0.5 nm followed by nonlinear growth in a transition period up to about 1.0 nm average thickness (Figure 3a). These thicknesses correspond to about 1.6 and 3.3 ML of TiO_2 respectively. Furthermore, the MCR-ALS analysis identifies a distinctive surface/interface component that is growing continuously through this time period, with a broad peak in concentration, about 0.2 nm, near the end of the transition period (Figure 4b). As we reported previously, the ALD TiO_2 films are essentially amorphous, containing crystalline domains no larger than about 1 nm.[38] One possibility is that the slow initial growth rate characteristic of the formation of prenucleation clusters on ZnO crosses over to faster growth predominantly on the surface of stabilized TiO_2 nuclei that achieve critical size. While the surface/interface component is observed to account for about 30% of the Ti during Stage I (Figure 4d), it does not accelerate during the transition period, as one would expect if they were on the surface of growing nuclei. Instead, the surface/interface component rolls over during the transition stage. Also, it slowly drops starting at the beginning of Stage II, consistent with coalescence by about 1.0 nm of growth. We therefore suggest that the transition phase is characterized by simultaneous growth

on the surface of some nuclei and formation of new prenucleation clusters. This fits with the early emergence of the bulk component in Stage I.

The surface/interface spectrum deduced from the MCR-ALS analysis provides insight to the important atomic scale motifs formed during the prenucleation Stage I and subsequently on the surface of the growing film. In our previous work, we have discovered that the ALD grown TiO_2 shells contained a large fraction of under-coordinated Ti^{4+} centers.[38, 39] In the analysis of the Ti *K*-edge XANES, the lower coordinated Ti^{4+} centers typically exhibit more pronounced pre-edge spectral features.[52] The surface/interface spectrum manifests a much stronger pre-edge peak as compared to the bulk film (Figure 4a). Therefore, we may conclude that the Ti-adsorbates during the prenucleation Stage I are substantially more enriched in under-coordinated Ti atomic motifs. The pre-edge location at 4969.5 eV is identical as the TTIP precursor vapor (Figure 4c), which has a tetrahedral symmetry, but is about 2 eV lower than the pre-edge of rutile TiO_2 (4971.3 eV, Supporting Information, Figure S10b), which features octahedral, six-fold Ti motifs. According to the empirical observation of Farges *et al.*, a shift of the pre-edge peak position toward lower energy by ~2 eV with respect to that of rutile TiO_2, together with a high pre-edge peak height, is characteristic of four-fold Ti.[52] These spectral features strongly suggest that the surface/interface features tetrahedral, four-fold Ti motifs.

However, the overall spectral shape, including the sharp pre-edge peak and the attenuated white line strength around 4990 eV, are clearly different from the measured spectrum for the TTIP precursor vapor (Figure 4c), which has a tetrahedral symmetry. This indicates that distinctive, low coordinated motifs are forming on the growth surface. As noted, similar spectra are observed for titanosilicates-1 (TS-1, Figure 4c) and other dilute TiO_2-SiO_2 aerogels, in which tetrahedral, four-fold Ti motifs have been recognized the main structural features.[49-51] Guided by this observation and simulation results for an open network structure of TiO_2 similar to silica polymorphs (Supplemental Material Figure S7), this strongly suggests that the

surface/interface spectrum corresponds to relatively isolated or lower density, networked, four-fold Ti motifs.

These four-fold motifs characterize the prenucleation stage and they persist throughout the full scope of the ALD growth. The concentration evolution of the surface/interface component in Figure 4b shows a clear rise during Stage I, as one would expect in the picture where prenucleation clusters are multiplying. Early in Stage II, the slow decrease in concentration of these motifs can be attribute to the smoothing of the ALD film after coalescence of nuclei.[53] Later in Stage II, there appears to be a steady state concentration of them with an equivalent thickness of 0.16 nm or 0.5 ML equivalent of TiO_2. The distribution of these motifs between the buried interface to ZnO and the outer surface under growth conditions cannot be determined. Since they emerge during the prenucleation stage, it is plausible that at least a portion of them remain at the buried interface. This is consistent with a simple structural model, namely Ti substituting for Zn in the open tetrahedral network of ZnO as part of a structural transition layer at the interface. At the TiO_2 growth surface in Stage II, 0.5 ML of four-fold Ti could be accommodated in a sparse array of centers with 0.4-0.5 nm separation. Alternatively, patches of corner shared tetrahedra could form. Overall, the presence of these motifs throughout all the stages of the growth strongly suggests that they play a specific role in hosting the reactions that incorporate new Ti into the growing film.

The kinetics measured on the faster, intra-cycle time scale helps us fit all the results into a picture of the titania ALD growth process. Figure 6 illustrates this picture through one cycle in the steady-state growth in Stage II. Prior to the TTIP pulse, there is a population of Ti centers we have identified as tetrahedrally coordinated that we designate by Ti_{4c} motifs (Figure 6a). During and immediately following the TTIP pulse, new Ti precursor molecules react with the surface, creating new Ti_{4c} motifs and simultaneously reacting with and driving the evolution of existing Ti centers on the surface to form more compact motifs that are five- or six-coordinated (designated by Ti_{5c}/Ti_{6c}). The intra-cycle kinetic data shows that the concentration of additional

Ti atoms on the surface has stabilized within about 5 seconds. Furthermore, the lack of any distinguishable spectral signature after 5 seconds suggests that there are no further structural rearrangements. However, it is possible that structural changes could occur if they did not alter the net mix of Ti-centered structural motifs detected in the spectra. The time-resolved differential spectra after 2.5 seconds show no pre-edge signature and beyond 5 seconds there is no discernable signal within the limitations of the remaining noise. We therefore suggest that the introduction of the H_2O pulse largely leads to cleavage of the remaining isopropoxy groups, replacing them with hydroxy groups and restoring the growth surface to the chemical state at the beginning of the ALD cycle. Such a change in the second neighbor environment is likely not detectible in the XANES signal. Other structural rearrangement cannot be excluded, but the concentration of the resultant reactants would be limited to a fraction of the identified surface/interface component. Finally, we note that the low density of these four-fold Ti motifs may be due to the steric influence of the isopropoxy groups.

Conclusion

A new picture for ALD growth of titania on ZnO has emerged from *in situ* synchrotron X-ray absorption near edge structure (XANES) experiments. Our analysis of the time dependent spectra reveals a distinct spectral signature corresponding to low-density, tetrahedral Ti motifs characteristic of the surface under growth conditions.

The methodology developed in this study enables continuous monitoring of ALD growth. The application to growth over a complex, 3D nano-architecture presents challenges compared with planar film growth. However, it is also an opportunity to leverage a roughly ten times increase in surface area. When combined with a unified set of data analysis approaches, the time sequence of XANES spectra elucidate the stages of the growth, disentangle spectral signatures characteristic of the bulk film as well as those indicative of the structure motifs

formed at the growth surface, and reveal the evolution of Ti on the growth surface within the time scale of the ALD cycle.

The *in situ* hard X-ray spectroscopy technique and data analytics methodology developed in this work offer a new and powerful toolset that is broadly adaptable for deciphering the structural evolution in a variety of atomic layer deposition and chemical vapor deposition processes. In particular, one of the unique strengths of ALD is conformal growth of films over nanostructured surfaces. XANES is one of the techniques that can provide atomic scale structural information for such samples with atomic specificity, benefiting from the increased surface area and high photon flux available for a broad range of X-ray edge energies.

Methods

Growth of ZnO nanowires: A ZnO nanowire array is grown over a silicon substrate using a seed-mediated hydrothermal method.[54, 55] A 3-nm ZnO seeding layer is deposited by pulsed layer deposition (PVD Products PLD/MBE 2300) at room temperature and is subsequently annealed in 1 atm oxygen at 400 °C for 10 minutes. The seeded substrate is then placed in the growth solution, an aqueous solution of zinc nitrate and hexamethylenetetramine. It is heated to 75°C, for 120 minutes. Prior to ALD TiO_2 coating, the nanowire array is sequentially treated by thermal annealing in O_2 at 500 °C and low pressure oxygen plasma cleaning, as described in our previous work.[38]

In situ XAS studies of TiO_2 ALD: The *in situ* Ti *K*-edge spectra are collected at the ISS beamline at NSLS-II. A fast scanning, liquid nitrogen cooled double crystal monochromator is used for continuous energy scans. An ion chamber is used to record the intensity of the incident beam and the fluorescence from the sample is captured by a PIPS (Passivated Implanted Planar Silicon) detector. Ti *K*-edge XANES spectra are collected in the energy range of 4920 – 5140 eV. A Veeco CNT Savannah S100 atomic ALD system is modified with a custom-designed

reaction chamber for *in situ* XAS measurement. The chamber and sample are heated to 150°C during TiO_2 deposition, while being purged by a continuous stream of N_2 at a base pressure of ~ 200 mTorr. The precursors are vapors of titanium isopropoxide (TTIP) and water. The precursors are alternatively introduced into the chamber in short pulses (~ 0.5 s), separated by an interval of 60 s. The Ti *K*-edge is at the limit of ISS energy range (4.8 – 32 keV), resulting a flux of ~10^{12} photons/s. Studies on heavier transition metals could offer improved sensitivity for probing the submonolayer components that characterize either the buried interface or the evolution of surface structure motifs during growth.

MCR analysis: The XANES data set is processed by MCR-ALS after background removal and normalization. The quantitative edge step is retained to capture Ti thickness information. The MCR algorithm decomposes the data set $\boldsymbol{D}$ to pure concentration $\boldsymbol{C}$ and pure spectra $\boldsymbol{S}^T$ through a bilinear factor decomposition $\boldsymbol{D} = \boldsymbol{C}\boldsymbol{S}^T + \boldsymbol{E}$, in which $\boldsymbol{E}$ is the error residual.[42, 43] The factor decomposition is performed by solving $\boldsymbol{C}$ and $\boldsymbol{S}^T$ alternatively using non-negative least squares regression. In the MCR-ALS, rotational ambiguity arises from the fact that an identity matrix $\boldsymbol{I} = \boldsymbol{T}\boldsymbol{T}^{-1}$ ($\boldsymbol{T}$ is a rotational matrix) can be inserted ($\boldsymbol{D} = \boldsymbol{C}\boldsymbol{T}\boldsymbol{T}^{-1}\boldsymbol{S}^T + \boldsymbol{E}$) leading to a new solution with identical error.[48] In addition, noise induced rotation can cause severe fluctuations in $\boldsymbol{C}$ and $\boldsymbol{S}^T$, interfering with convergence to physical solutions $\boldsymbol{C}$ and $\boldsymbol{S}^T$. The best approach to constrain MCR-ALS is typically problem dependent, although more general approaches to characterize the rotational ambiguity have been discussed.[48, 56] For the present problem, we find that a constraint that forces the concentrations to be smooth as a function of ALD cycle, as would be expected physically, leads to stable solutions with physical reference spectra. In each iteration of the MCR-ALS algorithm, after $\boldsymbol{C}$ is solved from $\boldsymbol{D}$, we fit the concentration profiles $\boldsymbol{C}$ to a B-spline. The B-spline is smooth and continuous by construction, and hence provides a more physically sound representation for concentration. The weights of the B-spline basis adapts progressively during the ALS iteration.[57] The fitting of each species is performed

independently. A detailed flow chart of the algorithm is illustrated in the Supporting Information, Figure S8. Finally, the MCR deconvoluted spectra are used as a basis to fit other spectra where needed using a non-negative least squares regression.

Intra-cycle transient spectrum: The recovery of transient spectrum $g(E,\tau)$ is enabled by setting the period of the ALD cycle (T_A) to be roughly twice as long as the XANES collection cycle (T_X). As such, about two XANES spectra are collected during each ALD cycle (Figure 5a). Consider a XANES data point collected at energy E_1 and delay time $\tau_1 < T_A/2$, i.e., within the TTIP half cycle. Then the X-ray energy scan will pass the same energy E_1 again a later time $\tau_1' = \tau_1 + T_X$. Since T_X is close to $T_A/2$, there is a high probability for the data point to fall within the H_2O half cycle, i.e., $\tau_1' > T_A/2$. We approximate $\mu(E_1, t_1' = kT_A + \tau_1')$ as the cycle end spectrum $\mu_k^s(E_1)$, assuming that the transient reaction gain $g(E,\tau > T_A/2) \approx 0$ is reproducible over the ALD cycles. By adapting Eq. 1, we calculate $g(E,\tau_1)$ as

$$g(E_1,\tau_1) = \mu(E, t_1 = kT_A + \tau_1) - \mu_k^s(E_1)$$
$$\approx \mu(E, t_1 = kT_A + \tau_1) - \mu(E, t_1' = kT_A + \tau_1'). \quad (2)$$

A dense sampling of the (E,τ) space is achieved by setting the T_A/T_X ratio distinct from any small-integer fraction.

Supporting Information

The Supporting Information is available free of charge on the ACS Publications website.

SEM and TEM images; XANES spectra of ALD TiO_2 shells and reference samples, including rutile and anatase; Normalized XANES spectrum at a few representative ALD cycles; Details of MCR-ALS analysis; Reconstructed intracycle transient spectrum $g(E,\tau)$ for delay time $\tau = 0 - 60$ s.

AUTHOR INFORMATION

Corresponding Author

* E-mail: mhyberts@bnl.gov;

* E-mail: istavitski@bnl.gov;

* E-mail: mzliu@bnl.gov

Acknowledgements

This research was carried out at Brookhaven National Laboratory (BNL) under Contract No. DE-SC0012704 where facilities used included those of the Center for Functional Nanomaterials (CFN) and 8-ID ISS (Inner Shell Spectroscopy) and 6-BM (BMM) beamlines in the National Synchrotron Light Source II, U.S. Department of Energy Office of Science User Facilities. This work used the computational resource of the Scientific Data and Computing Center, a component of the Computational Science Initiative at BNL. R. S. Li is supported by BNL LDRD Project No. 19-008. Helpful discussion with Dr. B. Ravel is greatly acknowledged.

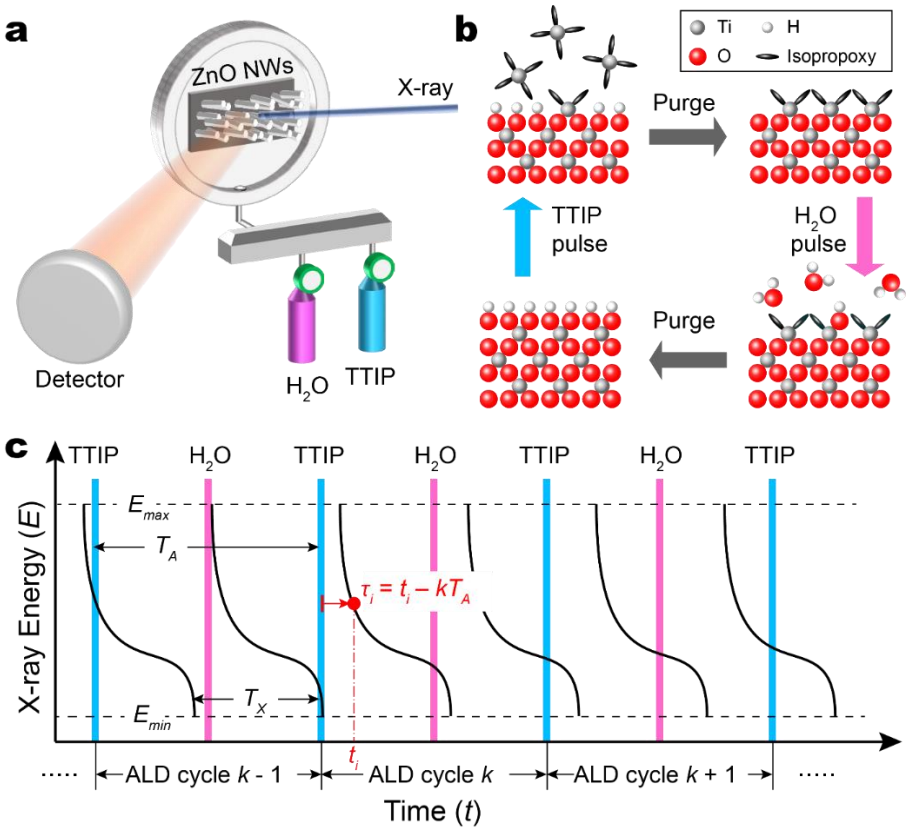

Figure 1. (a) A simplified sketch of the *in situ* XANES setup with the ALD chamber integrated with the beamline operation. The ZnO NWs substrate, placed in the ALD chamber, is simultaneously probed by the X-ray beam. XANES spectra are collected using a total fluorescence yield detector. (b) A simplified diagram illustrating the key steps in ALD of TiO_2, using TTIP and water as precursors. (c) The X-ray monochromator is repeatedly scanned over the spectral range, following a predetermined, non-uniform scanning trajectory (black line), with a periodicity of T_X. The ALD valve sequence is overlaid in vertical lines for pulses of TTIP (magenta) and H_2O (blue) precursors, with a periodicity of T_A. Within an ALD cycle k, a delay time from the TTIP pulse is defined as $\tau_i = t_i - kT_A$ for each time t_i.

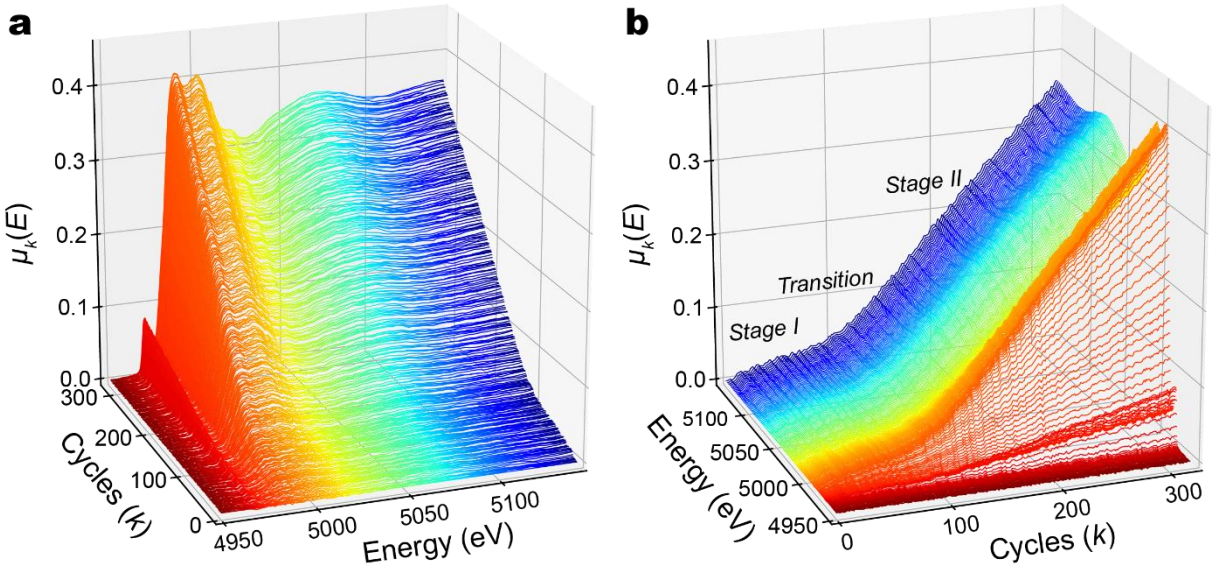

Figure 2. (a) *In situ* Ti-K edge XANES spectra of ALD grown TiO_2 shells on ZnO nanowires, binned according to ALD cycle number k as a series $\{\mu_k(E)\}$. (b) A transposed view of the same data, where each trace represents the $\mu_k(E)$ – k relation for each energy E. The overall kinetic profile is separated, based on the slopes, into three stages: an early, slower Stage I, a transition stage, and a fast Stage II that has a steady deposition rate.

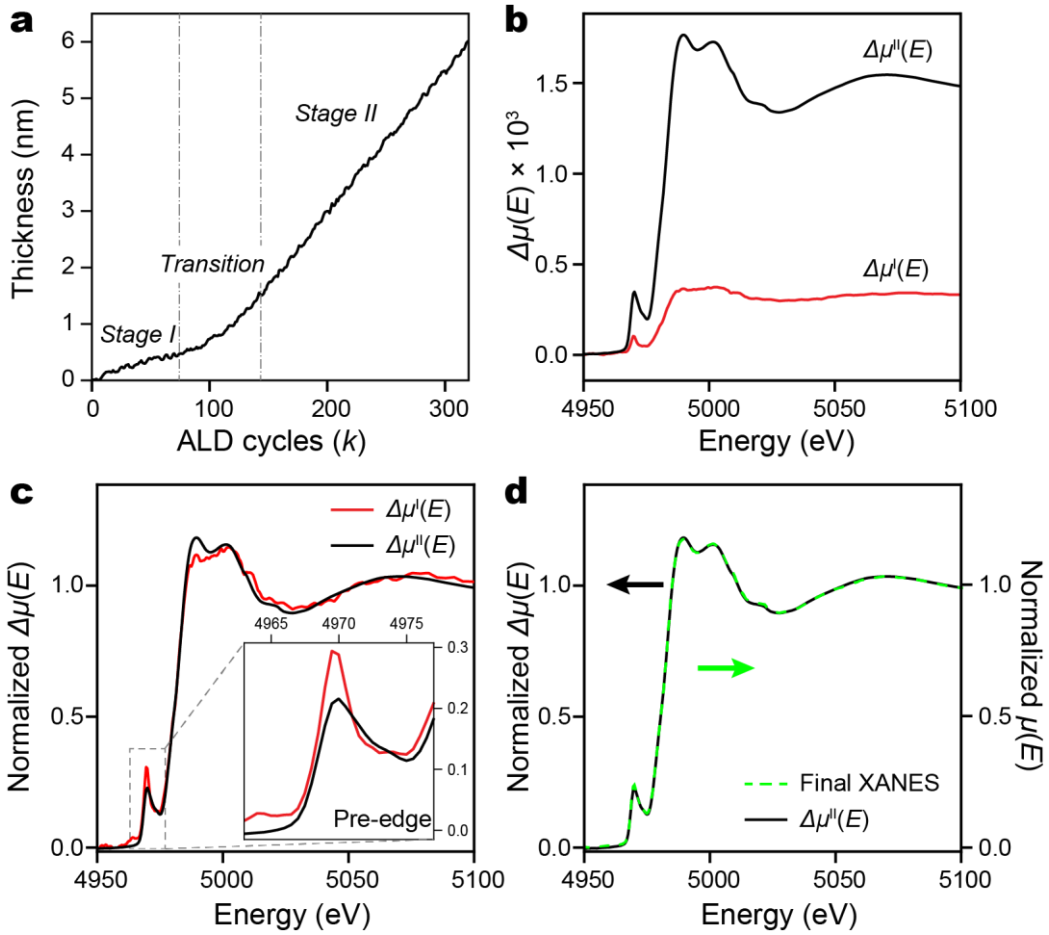

Figure 3. (a) Thickness of the TiO_2 shell versus number of elapsed ALD cycles determined by the XANES edge jump intensity. (b) Differential XANES spectra $\Delta\mu(E)$ from Stage I and Stage II. (c) $\Delta\mu(E)$ spectra normalized according to the edge jump of each spectrum. (*inset*) Zoom on the pre-edge region. (d) Differential XANES spectrum from stage II, $\Delta\mu^{\mathrm{II}}(E)$ compared with the XANES spectrum collected at the end of ALD (cycle 320).

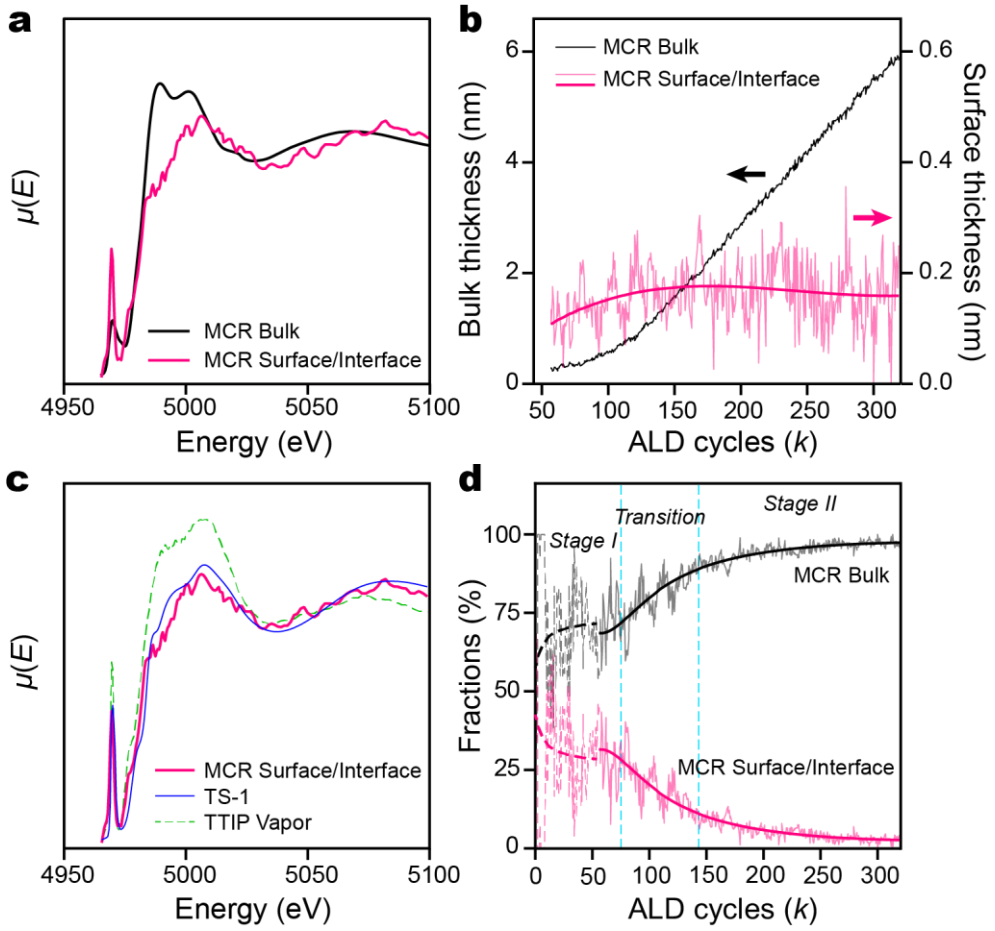

Figure 4. (a) Deconvoluted spectra and (b) equivalent thicknesses for TiO_2 bulk (black line) and surface/interface (magenta line) components obtained using MCR-ALS starting at ALD cycle k = 57. The smoothed surface/interface equivalent thickness (bold magenta line) is superposed on the raw profile. (c) MCR surface/interface spectrum is compared with the experimental XANES spectra of TTIP vapor (dashed green line, this work) and titanosilicate-1 (TS-1, blue line)[49]. (d) Evolution of the fractions of MCR bulk and surface/interface components throughout the growth. Results are also included based on fitting the early stage I data using the MCR spectra in (a), as detailed in the main text (k < 57, dashed lines).

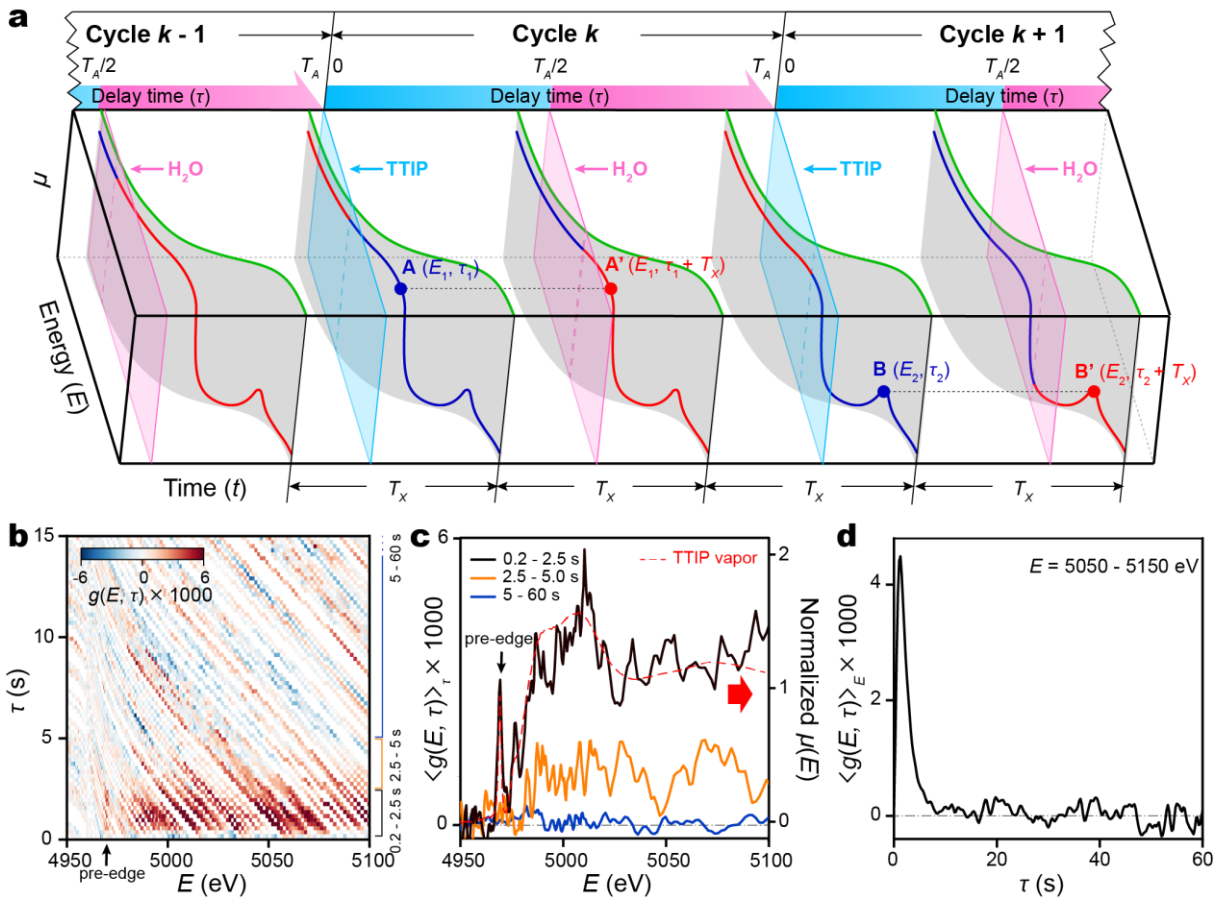

Figure 5. (a) Procedure to recover the transient spectrum $g(E,\tau)$ from the XANES spectral series, illustrated in a Cartesian space defined by time (t), photon energy (E), and X-ray absorption (μ). t axis is partitioned periodically into ALD cycles (T_A). Intracycle delay time τ starts with the TTIP pulse ($\tau = 0$, cyan planes) and includes the H_2O pulse ($\tau = T_A/2$, magenta planes). XANES spectra are shown on grey surfaces defined by the X-ray scanning trajectory (period T_X) with data colored according to whether that portion of the spectrum is collected in the TTIP and H_2O half cycles, blue and red respectively. Following Eq. (2), a contribution to the spectral transient $g(E_1,\tau_1)$ is given by $\mu(\mathbf{A}) - \mu(\mathbf{A'})$, with $\mathbf{A} = (E_1,\tau_1)$ in the TTIP half cycle and $\mathbf{A'} = (E_1,\tau_1 + T_X)$ in the H_2O half cycle. (b) Experimental 2D $g(E,\tau)$ map, accumulated from all such pairs across the full data set. The sharp pre-edge feature at 4968 eV is marked by an arrow. (c) XANES spectra of Ti transient species, determined by binning values of $g(E,\tau)$ over chosen delay time τ ranges. Measured XANES spectrum of vapor phase TTIP

is overlaid (red dashed line). (d) Coverage of Ti transient species measured by binning values of $g(E,\tau)$ over E, in the range of 5050 – 5150 eV, as a function of delay time τ.

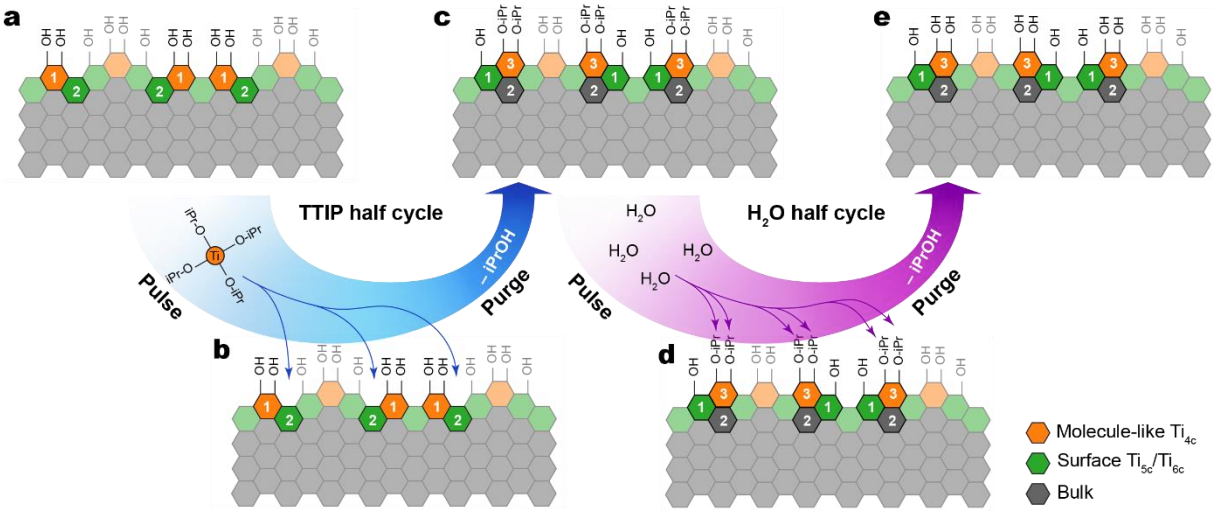

Figure 6. Evolution of TiO_2 surface atomic motif during one ALD cycle, based on results from MCR analysis and transient XANES spectroscopy. The TTIP half cycle starts from a hydroxyl-terminated surface (a) that is mixture of Ti_{5c}/Ti_{6c} and Ti_{4c} motifs. Different Ti atomic motifs are color coded (gray, bulk Ti; green, surface Ti_{5c}/Ti_{6c}; orange, surface Ti_{4c}). (b-c) Exposure to TTIP vapor creates new Ti_{4c} motifs (**3**), converts some old surface Ti_{4c} motifs into Ti_{5c}/Ti_{6c} motifs (**1**) through a condensation reaction that removes some of the isopropoxy, and part of the old surface turns into bulk (**2**). (d-e) In the H_2O half cycle, the remaining isopropoxy on the surface is hydrolyzed to form a hydroxyl-terminated surface (e), with little impact on the surface Ti atomic motifs otherwise and returning the surface to a condition equivalent to the starting point (a). In both half cycles, isopropanol is released through precursor-surface reactions.

References

1. Leskela, M.; Ritala, M., Atomic layer deposition chemistry: Recent developments and future challenges. *Angew. Chem.-Int. Ed.* **2003,** 42, 5548-5554.
2. George, S. M., Atomic Layer Deposition: An Overview. *Chem. Rev.* **2010,** 110, 111-131.
3. Johnson, R. W.; Hultqvist, A.; Bent, S. F., A brief review of atomic layer deposition: from fundamentals to applications. *Mater. Today* **2014,** 17, 236-246.
4. Knez, M.; Niesch, K.; Niinisto, L., Synthesis and surface engineering of complex nanostructures by atomic layer deposition. *Adv. Mater.* **2007,** 19, 3425-3438.
5. George, S. M.; Ott, A. W.; Klaus, J. W., Surface Chemistry for Atomic Layer Growth. *J. Phys. Chem.* **1996,** 100, 13121-13131.
6. Zaera, F., The surface chemistry of thin film atomic layer deposition (ALD) processes for electronic device manufacturing. *J. Mater. Chem.* **2008,** 18, 3521-3526.
7. Alaboson, J. M. P.; Wang, Q. H.; Emery, J. D.; Lipson, A. L.; Bedzyk, M. J.; Elam, J. W.; Pellin, M. J.; Hersam, M. C., Seeding Atomic Layer Deposition of High-k Dielectrics on Epitaxial Graphene with Organic Self-Assembled Monolayers. *ACS Nano* **2011,** 5, 5223-5232.
8. O'Neill, B. J.; Jackson, D. H. K.; Lee, J.; Canlas, C.; Stair, P. C.; Marshall, C. L.; Elam, J. W.; Kuech, T. F.; Dumesic, J. A.; Huber, G. W., Catalyst Design with Atomic Layer Deposition. *ACS Catal.* **2015,** 5, 1804-1825.
9. Hu, S.; Shaner, M. R.; Beardslee, J. A.; Lichterman, M.; Brunschwig, B. S.; Lewis, N. S., Amorphous TiO_2 coatings stabilize Si, GaAs, and GaP photoanodes for efficient water oxidation. *Science* **2014,** 344, 1005-1009.
10. Graniel, O.; Weber, M.; Balme, S.; Miele, P.; Bechelany, M., Atomic layer deposition for biosensing applications. *Biosens. Bioelectron.* **2018,** 122, 147-159.
11. Elam, J. W.; Nelson, C. E.; Grubbs, R. K.; George, S. M., Nucleation and growth during tungsten atomic layer deposition on SiO_2 surfaces. *Thin Solid Films* **2001,** 386, 41-52.
12. Wilson, C. A.; Grubbs, R. K.; George, S. M., Nucleation and Growth during Al_2O_3 Atomic Layer Deposition on Polymers. *Chem. Mat.* **2005,** 17, 5625-5634.
13. Skopin, E. V.; Rapenne, L.; Deschanvres, J. L.; Blanquet, E.; Ciatto, G.; Pithan, L.; Fong, D. D.; Richard, M. I.; Renevier, H., In situ x-ray studies of the incipient ZnO atomic layer deposition on $In_{0.53}Ga_{0.47}As$. *Phys. Rev. Mater.* **2020,** 4, 043403.
14. Knapas, K.; Ritala, M., In Situ Studies on Reaction Mechanisms in Atomic Layer Deposition. *Crit. Rev. Solid State Mater. Sci.* **2013,** 38, 167-202.
15. Elam, J. W.; Groner, M. D.; George, S. M., Viscous flow reactor with quartz crystal microbalance for thin film growth by atomic layer deposition. *Rev. Sci. Instrum.* **2002,** 73, 2981-2987.
16. Langereis, E.; Heil, S. B. S.; Knoops, H. C. M.; Keuning, W.; van de Sanden, M. C. M.; Kessels, W. M. M., In situspectroscopic ellipsometry as a versatile tool for studying atomic layer deposition. *J. Phys. D* **2009,** 42, 073001.
17. Van Bui, H.; Groenland, A. W.; Aarnink, A. A. I.; Wolters, R. A. M.; Schmitz, J.; Kovalgin, A. Y., Growth Kinetics and Oxidation Mechanism of ALD TiN Thin Films Monitored by In Situ Spectroscopic Ellipsometry. *J. Electrochem. Soc.* **2011,** 158, H214-H220.
18. Kessels, W. M. M.; Knoops, H. C. M.; Dielissen, S. A. F.; Mackus, A. J. M.; van de Sanden, M. C. M., Surface reactions during atomic layer deposition of Pt derived from gas phase infrared spectroscopy. *Appl. Phys. Lett.* **2009,** 95, 3.
19. Dendooven, J.; Pulinthanathu Sree, S.; De Keyser, K.; Deduytsche, D.; Martens, J. A.; Ludwig, K. F.; Detavernier, C., In Situ X-ray Fluorescence Measurements During Atomic

Layer Deposition: Nucleation and Growth of TiO_2 on Planar Substrates and in Nanoporous Films. *J. Phys. Chem. C* **2011,** 115, 6605-6610.
20. Skopin, E. V.; Rapenne, L.; Roussel, H.; Deschanvres, J.-L.; Blanquet, E.; Ciatto, G.; Fong, D. D.; Richard, M.-I.; Renevier, H., The initial stages of ZnO atomic layer deposition on atomically flat $In_{0.53}Ga_{0.47}As$ substrates. *Nanoscale* **2018,** 10, 11585-11596.
21. Rehr, J. J.; Albers, R. C., Theoretical approaches to x-ray absorption fine structure. *Rev. Mod. Phys.* **2000,** 72, 621-654.
22. Wende, H., Recent advances in x-ray absorption spectroscopy. *Rep. Prog. Phys.* **2004,** 67, 2105-2181.
23. Dendooven, J.; Solano, E.; Minjauw, M. M.; Kerckhove, K. V. d.; Coati, A.; Fonda, E.; Portale, G.; Garreau, Y.; Detavernier, C., Mobile setup for synchrotron based in situ characterization during thermal and plasma-enhanced atomic layer deposition. *Rev. Sci. Instrum.* **2016,** 87, 113905.
24. Devloo-Casier, K.; Ludwig, K. F.; Detavernier, C.; Dendooven, J., In situ synchrotron based x-ray techniques as monitoring tools for atomic layer deposition. *J. Vac. Sci. Technol. A* **2014,** 32, 010801.
25. Setthapun, W.; Williams, W. D.; Kim, S. M.; Feng, H.; Elam, J. W.; Rabuffetti, F. A.; Poeppelmeier, K. R.; Stair, P. C.; Stach, E. A.; Ribeiro, F. H.; Miller, J. T.; Marshall, C. L., Genesis and Evolution of Surface Species during Pt Atomic Layer Deposition on Oxide Supports Characterized by in Situ XAFS Analysis and Water−Gas Shift Reaction. *J. Phys. Chem. C* **2010,** 114, 9758-9771.
26. Dadlani, A.; Acharya, S.; Trejo, O.; Nordlund, D.; Peron, M.; Razavi, J.; Berto, F.; Prinz, F. B.; Torgersen, J., Revealing the Bonding Environment of Zn in ALD Zn(O,S) Buffer Layers through X-ray Absorption Spectroscopy. *ACS Appl. Mater. Interfaces* **2017,** 9, 39105-39109.
27. Trejo, O.; Dadlani, A. L.; De La Paz, F.; Acharya, S.; Kravec, R.; Nordlund, D.; Sarangi, R.; Prinz, F. B.; Torgersen, J.; Dasgupta, N. P., Elucidating the Evolving Atomic Structure in Atomic Layer Deposition Reactions with in Situ XANES and Machine Learning. *Chem. Mater.* **2019,** 31, 8937-8947.
28. Klug, J. A.; Weimer, M. S.; Emery, J. D.; Yanguas-Gil, A.; Seifert, S.; Schlepütz, C. M.; Martinson, A. B. F.; Elam, J. W.; Hock, A. S.; Proslier, T., A modular reactor design for in situ synchrotron x-ray investigation of atomic layer deposition processes. *Rev. Sci. Instrum.* **2015,** 86, 113901.
29. Boichot, R.; Tian, L.; Richard, M. I.; Crisci, A.; Chaker, A.; Cantelli, V.; Coindeau, S.; Lay, S.; Ouled, T.; Guichet, C.; Chu, M. H.; Aubert, N.; Ciatto, G.; Blanquet, E.; Thomas, O.; Deschanvres, J. L.; Fong, D. D.; Renevier, H., Evolution of Crystal Structure During the Initial Stages of ZnO Atomic Layer Deposition. *Chem. Mater.* **2016,** 28, 592-600.
30. Filez, M.; Poelman, H.; Ramachandran, R. K.; Dendooven, J.; Devloo-Casier, K.; Fonda, E.; Detavernier, C.; Marin, G. B., In situ XAS and XRF study of nanoparticle nucleation during O_3-based Pt deposition. *Catal. Today* **2014,** 229, 2-13.
31. Fuoss, P. H.; Kisker, D. W.; Lamelas, F. J.; Stephenson, G. B.; Imperatori, P.; Brennan, S., Time-resolved x-ray scattering studies of layer-by-layer epitaxial growth. *Phys. Rev. Lett.* **1992,** 69, 2791-2794.
32. Heald, S. M.; Brewe, D. L.; Stern, E. A.; Kim, K. H.; Brown, F. C.; Jiang, D. T.; Crozier, E. D.; Gordon, R. A., XAFS and micro-XAFS at the PNC-CAT beamlines. *J. Synchrotron Rad.* **1999,** 6, 347-349.
33. Jenichen, B.; Braun, W.; Kaganer, V. M.; Shtukenberg, A. G.; Däweritz, L.; Schulz, C.-G.; Ploog, K. H.; Erko, A., Combined molecular beam epitaxy and diffractometer system for in situ x-ray studies of crystal growth. *Rev. Sci. Instrum.* **2003,** 74, 1267-1273.

34. Andersen, T. K.; Cook, S.; Benda, E.; Hong, H.; Marks, L. D.; Fong, D. D., Development of a hybrid molecular beam epitaxy deposition system for in situ surface x-ray studies. *Rev. Sci. Instrum.* **2018,** 89, 033905.
35. Motamedi, P.; Bosnick, K.; Cadien, K.; Hogan, J. D., In Situ Synchrotron X-Ray Diffraction Analysis of Phase Transformation in Epitaxial Metastable hcp Nickel Thin Films, Prepared via Plasma-Enhanced Atomic Layer Deposition. *Adv. Mater. Interfaces* **2018,** 5, 1800957.
36. Young, M. J.; Bedford, N. M.; Yanguas-Gil, A.; Letourneau, S.; Coile, M.; Mandia, D. J.; Aoun, B.; Cavanagh, A. S.; George, S. M.; Elam, J. W., Probing the Atomic-Scale Structure of Amorphous Aluminum Oxide Grown by Atomic Layer Deposition. *ACS Appl. Mater. Interfaces* **2020,** 12, 22804-22814.
37. Geyer, S. M.; Methaapanon, R.; Johnson, R. W.; Kim, W.-H.; Campen, D. G. V.; Metha, A.; Bent, S. F., An atomic layer deposition chamber for in situ x-ray diffraction and scattering analysis. *Rev. Sci. Instrum.* **2014,** 85, 055116.
38. Yan, D. H.; Topsakal, M.; Selcuk, S.; Lyons, J. L.; Zhang, W. R.; Wu, Q. Y.; Waluyo, I.; Stavitski, E.; Attenkofer, K.; Yoo, S.; Hybertsen, M. S.; Lu, D. Y.; Stacchiola, D. J.; Liu, M. Z., Ultrathin Amorphous Titania on Nanowires: Optimization of Conformal Growth and Elucidation of Atomic-Scale Motifs. *Nano Lett.* **2019,** 19, 3457-3463.
39. Yan, D.; Topsakal, M.; Selcuk, S.; Lyons, J. L.; Zhang, W.; Wu, Q.; Waluyo, I.; Stavitski, E.; Attenkofer, K.; Yoo, S.; Hybertsen, M. S.; Lu, D.; Stacchiola, D. J.; Liu, M., Correction to Ultrathin Amorphous Titania on Nanowires: Optimization of Conformal Growth and Elucidation of Atomic-Scale Motifs. *Nano Lett.* **2020,** 20, 1475-1475.
40. Das, C.; Henkel, K.; Tallarida, M.; Schmeißer, D.; Gargouri, H.; Kärkkänen, I.; Schneidewind, J.; Gruska, B.; Arens, M., Thermal and plasma enhanced atomic layer deposition of TiO_2: Comparison of spectroscopic and electric properties. *J. Vac. Sci. Technol. A* **2015,** 33, 01A144.
41. Ritala, M.; Leskela, M.; Niinisto, L.; Haussalo, P., Titanium isopropoxide as a precursor in atomic layer epitaxy of titanium dioxide thin films. *Chem. Mater.* **1993,** 5, 1174-1181.
42. Tauler, R.; Kowalski, B.; Fleming, S., Multivariate curve resolution applied to spectral data from multiple runs of an industrial process. *Anal. Chem.* **1993,** 65, 2040-2047.
43. de Juan, A.; Tauler, R., Chapter 2 - Multivariate Curve Resolution-Alternating Least Squares for Spectroscopic Data. In *Data Handling in Science and Technology*, Ruckebusch, C., Ed. Elsevier: 2016; Vol. 30, pp 5-51.
44. Ruckebusch, C.; Blanchet, L., Multivariate curve resolution: A review of advanced and tailored applications and challenges. *Anal. Chim. Acta* **2013,** 765, 28-36.
45. Lin, C.-H.; Topsakal, M.; Sun, K.; Bai, J.; Zhao, C.; Dooryhee, E.; Northrup, P.; Gan, H.; Lu, D.; Stavitski, E.; Chen-Wiegart, Y.-c. K., Operando structural and chemical evolutions of TiS_2 in Na-ion batteries. *J. Mater. Chem. A* **2020,** 8, 12339-12350.
46. Voronov, A.; Urakawa, A.; Beek, W. v.; Tsakoumis, N. E.; Emerich, H.; Rønning, M., Multivariate curve resolution applied to in situ X-ray absorption spectroscopy data: An efficient tool for data processing and analysis. *Anal. Chim. Acta* **2014,** 840, 20-27.
47. Staniuk, M.; Hirsch, O.; Kränzlin, N.; Böhlen, R.; van Beek, W.; Abdala, P. M.; Koziej, D., Puzzling Mechanism behind a Simple Synthesis of Cobalt and Cobalt Oxide Nanoparticles: In Situ Synchrotron X-ray Absorption and Diffraction Studies. *Chem. Mater.* **2014,** 26, 2086-2094.
48. Malik, A.; Tauler, R., Chapter 4 - Ambiguities in Multivariate Curve Resolution. In *Data Handling in Science and Technology*, Ruckebusch, C., Ed. Elsevier: 2016; Vol. 30, pp 101-133.
49. Grunwaldt, J.-D.; Beck, C.; Stark, W.; Hagen, A.; Baiker, A., In situ XANES study on TiO_2-SiO_2 aerogels and flame made materials. *Phys. Chem. Chem. Phys.* **2002,** 4, 3514-3521.

50. Prestipino, C.; Bonino, F.; Usseglio, S.; Damin, A.; Tasso, A.; Clerici, M. G.; Bordiga, S.; D'Acapito, F.; Zecchina, A.; Lamberti, C., Equilibria between Peroxo and Hydroperoxo Species in the Titanosilicates: An In Situ High-Resolution XANES Investigation. *ChemPhysChem* **2004,** 5, 1799-1804.
51. Signorile, M.; Braglia, L.; Crocellà, V.; Torelli, P.; Groppo, E.; Ricchiardi, G.; Bordiga, S.; Bonino, F., Titanium Defective Sites in TS-1: Structural Insights by Combining Spectroscopy and Simulation. *Angew. Chem. Int. Ed.* **2020,** 59, 18145-18150.
52. Farges, F.; Brown, G. E.; Rehr, J. J., Ti *K*-edge XANES studies of Ti coordination and disorder in oxide compounds: Comparison between theory and experiment. *Phys. Rev. B* **1997,** 56, 1809-1819.
53. Wind, R. W.; Fabreguette, F. H.; Sechrist, Z. A.; George, S. M., Nucleation period, surface roughness, and oscillations in mass gain per cycle during W atomic layer deposition on Al_2O_3. *J. Appl. Phys.* **2009,** 105, 074309.
54. Greene, L. E.; Law, M.; Goldberger, J.; Kim, F.; Johnson, J. C.; Zhang, Y. F.; Saykally, R. J.; Yang, P. D., Low-temperature wafer-scale production of ZnO nanowire arrays. *Angew. Chem.-Int. Ed.* **2003,** 42, 3031-3034.
55. Greene, L. E.; Law, M.; Tan, D. H.; Montano, M.; Goldberger, J.; Somorjai, G.; Yang, P. D., General route to vertical ZnO nanowire arrays using textured ZnO seeds. *Nano Lett.* **2005,** 5, 1231-1236.
56. Tauler, R., Calculation of maximum and minimum band boundaries of feasible solutions for species profiles obtained by multivariate curve resolution. *J. Chemometrics* **2001,** 15, 627-646.
57. Prautzsch, H.; Boehm, W.; Paluszny, M., B-spline representation. In *Bézier and B-Spline Techniques*, Springer Berlin Heidelberg: Berlin, Heidelberg, 2002; pp 59-75.

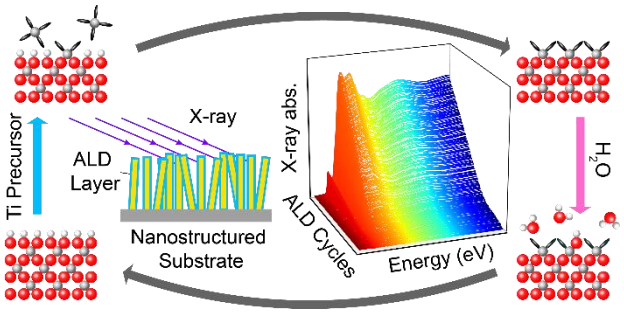

TOC Graphics.